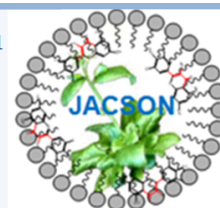
Content lists available at www.jacsonline.org/D176750082-LROR/ JACSONline GP, DOI:10.22341

Journal of Applied Chemical Science

Journal homepage: www.jacsonline.org/journals/jacson/

Synthesis, Evaluation, Modeling and Simulation of Nanopore NaA Zeolite Membranes for Application in Ethanol Separation

Mansoor Kazemimoghadam^{1*} and Zahra Amiri Rigi²

¹Department of Chemical Engineering, Malek-Ashtar University of Technology, Tehran, IRAN, ²Department of Chemical Engineering, South Tehran Branch, Islamic Azad University, Tehran, IRAN

Article history: Received in revised form Oct. 27, 2017

Accepted February 25, 2017

Available online June 20, 2018

Cite this article as: Kazemimoghadam M and Rigi ZA. Synthesis, Evaluation, Modeling and Simulation of Nanopore NaA Zeolite Membranes for Application in Ethanol Separation. J Applied Chem. Sci. 2018, 5(2): 445-458

DOI : <https://dx.doi.org/10.22341/iacs.on.00501p445>

p-ISSN: 2089-6328, e-ISSN: 2580-1953 © 2018 JACSONline GP. All right served



The JACSONline Group Publisher publishes the work of Jacson-Journal of Applied Chemical Science eISSN: 2580-1953/pISSN: 2089-6328 under the licensing of a Creative Commons Attribution-NonCommercial-ShareAlike 3.0 Unported License. Authors retain the copyright to their work. Users may read, copy, and distribute the work in any medium provided the authors and the journal are appropriately credited. The users may not use the material for commercial purposes.

ABSTRACTS

Zeolite membranes have uniform and molecular-sized pores that separate molecules based on the differences in the molecules' adsorption and diffusion properties. Strong electrostatic interaction between ionic sites and water molecules (due to its highly polar nature) makes the zeolite NaA membrane very hydrophilic. Zeolite NaA membranes are thus well suited for the separation of liquid-phase mixtures by pervaporation. In this study, experiments were conducted with various ethanol–water mixtures (1–20 wt. %) at 25 °C. Total flux for ethanol–water mixtures was found to vary from 0.331 to 0.229 kg/m².h with increasing ethanol concentration from 1 to 20 wt.%. Ionic sites of the NaA zeolite matrix play a very important role in water transport through the membrane. These sites act both as water sorption and transport sites. Surface diffusion of water occurs in an activated fashion through these sites. The precise Nano-porous structure of the zeolite cage helps in a partial molecular sieving of the large solvent molecules leading to high separation factors. A comparison between experimental flux and calculated flux using Stephan Maxwell (S.M.) correlation was made and a linear trend was found to exist for water flux through the membrane with ethanol concentration. A comprehensive model also was proposed for the ethanol-water pervaporation by Finite Element Method (FEM). The 2D model was masterfully capable of predicting water concentration distribution within both the membrane and the feed side of the pervaporation membrane module.

Keywords: nanopores, pervaporation, ethanol separation, zeolite NaA membrane, FEM simulation

* Corresponding author: mzkazemi@gmail.com

1. Introduction

Ethanol is a very important and commonly used solvent in biopharmaceutical and chemical industries. It is widely applied as a disinfectant in medical products, as fuel in rockets and engines and as a feedstock for synthesis of other organic chemicals such as acetic acid, butanol and ethyl ester (Díaz and Tost, 2016; Nour et al., 2017; Klinov et al., 2017). Thus, it is very important to treat ethanol wastewaters to separate this valuable material and prevent its wasting.

Separation of ethanol from its aqueous mixture can be performed through conventional distillation. However, purification of ethanol solution is very difficult by distillation mainly because it forms an azeotrope with water once it reaches 89.4 mole % at 78 °C and atmospheric pressure. Thus, azeotropic distillation must be applied for this purpose. However, azeotropic distillation is more energy demanding than traditional distillation. Besides that, benzene, a highly carcinogenic and toxic substance will be produced in this process, which is considered a major health concern (Hoof et al., 2006; Amnuaypanich et al., 2009).

Instead, pervaporation is an economical filtration technique compared to conventional distillation, especially in

processes involving azeotropes, isomers and removal or recovery of trace substances. This is mainly because that only a fraction of the solution that needs to be separated is vaporized in pervaporation. Additionally, high flux rate of pervaporation makes this method an efficient purification procedure resulting in energy cost saving. Table 1 shows the amount of energy demanded by different separation processes in ethanol dehydration. In terms of energy requirement, pervaporation is an obvious choice in ethanol–water filtration (Sato et al., 2007; Li et al., 2007; Xia et al., 2016; Li et al., 2017). Aside from consuming lower energy, capital cost of pervaporation operation is considerably lower, which makes it again more effective compared to distillation. Pervaporation has attracted great attention not only for its cost-effective

Table 1. Energy requirements for ethanol dehydration

Purification (Wt. %)	Energy required (kJ/kg EtOH)	Process
8.0–99.5	10376	Distillation
95.0–99.5	3305	Azeotropic distillation
95.0–99.5	423	Pervaporation

features, but also for its simplicity and safe operation. In fact, the main tools applied in pervaporation systems are a vacuum pump creating the required driving force and a membrane separating the solution. Furthermore, pervaporation eliminates the use of toxic materials such as benzene and thus is a promising alternative for energy consuming distillation systems in filtering azeotropic mixtures. Hence, relatively mild operating conditions and high effectiveness make pervaporation an appropriate technique for such separations (Yin et al., 2017; Jiang et al., 2017; Narkkun et al., 2017; Santoro et al., 2017).

In general, polymeric membranes can be applied for pervaporation dehydration of organic solutions such as ethanol-water mixture. However, these membranes are not suitable for applications involving harsh chemicals due to the membrane chemical instability. In this regard, recent chemical- and temperature resistant hydrophilic ceramic membranes have been developed, making it possible to overcome the limitations of polymeric membranes (Pera-Titus et al., 2006; Kondo et al., 2010; Yu et al., 2017). Since zeolites are most hydrophilic and have well-defined open crystal structures with a pore size of several angstroms, they are another candidate for the pervaporation dehydration of highly concentrated ethanol aqueous solution. These unique structural characteristics and hydrophilic nature have rendered zeolite materials possessing pronounced molecular sieving effect and selective adsorption capability (i.e., appreciated separation performance). Therefore, zeolites can be extensively used in removal of volatile organic chemicals from air streams, separation of isomers and mixtures of gases, shape-selective catalysis and ion exchange.

Zeolitic membranes offer several advantages over polymeric ones. Firstly, they do not swell significantly compared to the polymeric membranes. Secondly, they have uniform molecular-sized pores that provide differential transport rates and molecular sieve effects. Thirdly, the zeolitic structures are more chemically stable and tolerant to severe separation conditions such as strong solvents or low pH solutions. Last but not least, zeolites are thermally stable up to high temperatures of 1000 °C (Sorenson et al., 2017; Liu et al., 2017).

In pervaporation, the feed mixture is contacted with a perm-selective nonporous membrane. Separation is generally explained by the steps of sorption into, diffusion through and desorption from the membrane. The latter is usually considered fast and taking place at equilibrium while diffusion is kinetically controlled and the slowest step of the process. Permeation is dependent on the sorption and diffusion steps. The driving force for the separation is created by maintaining a pressure lower than the saturation pressure on the permeate side of the membrane. The mechanism of filtration is usually described in terms of sorption-diffusion processes (Lin et al., 2009; Qu et al., 2010; Das and Ray, 2013; Das and Ray, 2016).

A great deal still remains to be known about the transport mechanisms of various species through zeolite membranes. The transport mechanism of aqueous species

through zeolitic materials is more complex than through polymeric membranes, since it can involve movement through both molecularly selective zeolite micro crystals as well as less selective interstitial regions. This produces a complex morphology and transport situation.

Extensive studies have been conducted for mass transfer modeling of pervaporation systems (Rezakazemi et al., 2011; Qiao et al., 2011; Moulik et al., 2015; Liu et al., 2015; Moulik et al., 2016; Samei et al., 2016; Rom et al., 2016; Jain et al., 2017). Recently Rezakazemi et al. (2011) proposed a model for pervaporation separation of water/ethylene glycol solution based on solving equations of mass and momentum conservation (Navier-Stokes equations) with Finite Element Method (FEM). Effect of temperature and velocity was investigated in their research and their results were in good agreement with experimental data. After Rezakazemi et al. (2011), Moulik et al. (2015) used the same approach and developed a steady state model to predict mass transfer of monomethylhydrazine and un-symmetrical dimethylhydrazine solutions by pervaporation (Moulik et al., 2015). Their results were also in reasonable accordance with empirical data. Nonetheless, their model was not comprehensive, since they only modeled the membrane section of the module. The effect of dimensional factors relating to the geometry of the system is also neglected in their study.

So far, few attempts have been done to simulate ethanol-water pervaporation. This paper focuses on purification of ethanol-water mixtures using hydrophilic zeolite membranes in pervaporation process. The objective of this study was to develop effective models for providing a deep insight into the dehydration of ethanol-water mixtures with pervaporation technology. A comparison between experimental flux and calculated flux using S.M. correlation was made and a linear trend was found to exist for water flux through the membrane with ethanol concentration. Impact of the differences in the transport mechanisms on pervaporation flux and selectivity was also discussed. A mathematical model based on CFD technique was finally proposed and the effect of different membrane's dimensions, initial ethanol concentration and feed flow rates on water concentration was investigated to find the optimum operation condition. Proposed model was distinctively capable of predicting concentration distribution in both membranes, feed subdomains, and provided a perfect understanding of the effect of various operating condition on the membrane performance.

The hydrophilic membranes used in this research were composite zeolite NaA membranes. The membranes were basically made of an active NaA layer, deposited on a ceramic porous mullite support. The active NaA layer is responsible for high separation factors achieved in pervaporation of ethanol mixtures. The structure of zeolite NaA is shown in Fig. 1.

As shown in the figure, the aluminosilicate framework of zeolite NaA is generated by placing truncated octahedrons (b-cage) at eight corners of a cube and each edge of the cube is formed by joining two b-cages by a D4R linkage. Each b-cage

encloses a cavity with a free diameter of 0.66 nm and each unit cell encloses a larger cavity (α-cage) enclosing a free diameter of 1.14 nm. There are two interconnecting, three-dimensional channels in zeolite NaA: (i) connected α-cages, 1.14 nm in diameter, separated by 0.42 nm apertures, (ii) β-cages, alternating with α-cages separated by 0.22 nm apertures. Thus, molecules smaller than 0.42 nm in diameter can diffuse easily through the nanopores of the zeolite. Moreover, position of sodium ions in unit cells is important since these ions act as the sites for water sorption and transport through the membrane. For a typical zeolite, a unit cell having the composition $\text{Na}_{12}\text{Al}_{12}\text{Si}_{12}\text{O}_{48}\cdot 27\text{H}_2\text{O}$, eight (out of 12) sodium ions are located inside α-cage and four ions are located in β-cages.

Truncated Octahedrons (β-cages)

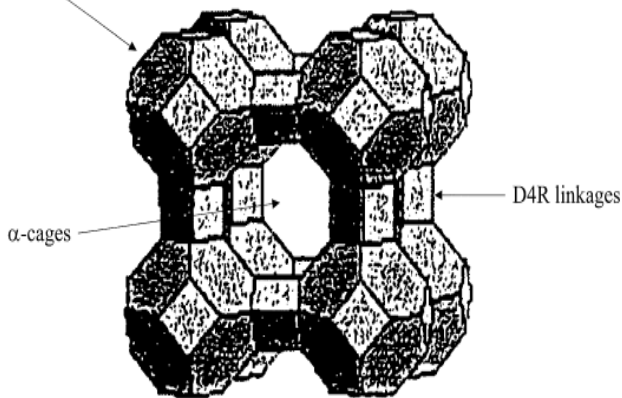


Fig. 1. Repeating unit of the zeolite NaA

Transport of solvent species (mainly water) through the zeolite matrix comprises of three steps: (i) strong adsorption of the species into a cage from feed side, (ii) surface diffusion of the species from cage to cage and (iii) vaporization of the species to permeate side. Normally, any physical adsorption process includes both van der Waals dispersion-repulsion forces and electrostatic forces comprising of polarization, dipole and quadruple interactions. However, since the zeolites have an ionic structure, the electrostatic forces become very large in adsorption of polar molecules like H_2O . This effect is manifested in the fact that heat of adsorption of water into zeolitic adsorbents is unusually high (25–30 kcal/mole).

Researchers have extended the dusty-gas model approach to describe the surface-diffusion of molecules into a zeolite surface. The vacant sites are assumed to be the $(n+1)$ pseudo-species in the system and S.M. Equation is used to correlate surface chemical potential gradient to flux of the various species, as shown in Eq. (1):

$$-\nabla\mu_i = RT \sum_{k=1}^n \theta_k \frac{(v_i - v_{n+1})}{D_{ik}^s} + RT\theta_{n+1} \frac{(v_i - v_{n+1})}{D_{i,n+1}^s}, \quad i = 1, 2, \dots, n \quad (1)$$

For two components denoted by 1 and 2, diffusing in a zeolite pore where the vacant sites are represented by v , individual component equations can be written as shown in Eqs. (2) and (3) (velocity of the sites v_v is equal to 0). It is also conventional to define surface diffusivity D_{iv}^s as the ratio of $D_{i,n+1}^s$ and θ_{n+1} .

$$-\frac{\nabla\mu_1}{RT} = \left[\frac{\theta_2(v_1 - v_2)}{D_{12}^s} + \frac{v_1}{D_{1v}^s} \right] \quad (2)$$

$$-\frac{\nabla\mu_2}{RT} = \left[\frac{\theta_1(v_2 - v_1)}{D_{21}^s} + \frac{v_2}{D_{2v}^s} \right] \quad (3)$$

Surface flux of each species through the zeolite pore is represented by Eqs. (4) and (5), where ρ_P is density of the zeolite, ϵ is porosity, q_{sat}^i is maximum possible sorption of component i into the zeolite, θ_i is site occupancy of species i and v_i is velocity of component i through the pores.

$$J_1^s = \rho_P \epsilon q_{sat}^1 \theta_1 v_1 \quad (4)$$

$$J_2^s = \rho_P \epsilon q_{sat}^2 \theta_2 v_2 \quad (5)$$

By assuming that there is no counter diffusion or coupling between the two species (D_{12}^s and $D_{21}^s \rightarrow \infty$), Eqs. (2) and (3) can be further simplified to Eqs. (6) and (7):

$$-\frac{\nabla\mu_1}{RT} = \frac{J_1^s}{\rho_P \epsilon q_{sat}^1 \theta_1 D_{1v}^s} \quad (6)$$

$$-\frac{\nabla\mu_2}{RT} = \frac{J_2^s}{\rho_P \epsilon q_{sat}^2 \theta_2 D_{2v}^s} \quad (7)$$

From basic thermodynamics, chemical potential gradients $\nabla\mu_1$ and $\nabla\mu_2$ can be represented as gradients of the site occupancy of each species by the following equations:

$$-\frac{\theta_1 \nabla\mu_1}{RT} = \theta_1 \frac{\partial \ln a_1}{\partial \theta_1} \frac{d\theta_1}{dz} + \theta_1 \frac{\partial \ln a_1}{\partial \theta_2} \frac{d\theta_2}{dz} \quad (8)$$

$$-\frac{\theta_2 \nabla\mu_2}{RT} = \theta_2 \frac{\partial \ln a_2}{\partial \theta_2} \frac{d\theta_2}{dz} + \theta_2 \frac{\partial \ln a_2}{\partial \theta_1} \frac{d\theta_1}{dz} \quad (9)$$

With equating Eqs. (6) and (7) with Eqs. (8) and (9), respectively, the following equations will be obtained:

$$J_1^s = -\rho_P \epsilon q_{sat}^1 D_{1v}^s \left[\theta_1 \frac{\partial \ln a_1}{\partial \theta_1} \frac{d\theta_1}{dz} + \theta_1 \frac{\partial \ln a_1}{\partial \theta_2} \frac{d\theta_2}{dz} \right] \quad (10)$$

$$J_2^s = -\rho_P \epsilon q_{sat}^2 D_{2v}^s \left[\theta_2 \frac{\partial \ln a_2}{\partial \theta_2} \frac{d\theta_2}{dz} + \theta_2 \frac{\partial \ln a_2}{\partial \theta_1} \frac{d\theta_1}{dz} \right] \quad (11)$$

The above two equations describe flux of each component through the zeolite pore. Nature of the functions, $\left(\frac{\partial \ln a_1}{\partial \theta_1}\right)$, $\left(\frac{\partial \ln a_1}{\partial \theta_2}\right)$, $\left(\frac{\partial \ln a_2}{\partial \theta_1}\right)$ and $\left(\frac{\partial \ln a_2}{\partial \theta_2}\right)$ depends on the nature of the sorption isotherm of each compound into the zeolite. Diffusivities D_{1v}^s and D_{2v}^s are also dependent on the site occupancies, θ_1 and θ_2 . Thus, to be able to model flux of each component through the zeolite cages, knowledge of both diffusion and sorption characteristics is essential. For zeolites with narrow pores (as in the case of zeolite NaA), single file diffusion can be assumed to take place. In the case of single file diffusion, only one molecule can diffuse through the cross-section of the pore at any given time. The S.M. surface diffusivity (D_{1v}^s) depends linearly on the vacant sites θ_v as shown below:

$$D_{1v}^s = D_{1v}^s(0)\theta_v \quad (12)$$

A Langmuirian type of sorption isotherm (for pure water into zeolite sites) to predict activity (a_w) in the zeolite for a given site, occupancy (θ_w) can be assumed:

$$a_w = \frac{A\theta_w}{1 - \theta_w} \quad (13)$$

For pure water-zeolite system, there is no second component and Eqs. (11)-(13) can be used to obtain the pure water flux equation as:

$$J_w^s = \rho \varepsilon q_{sat}^w D_{wV}^s(0) \frac{d\theta_w}{dz} \quad (14)$$

Integrating the above equation between the limits $z=0$, $q_w=q_{w,f}$ and $z=\delta$, $\theta_w=\theta_{w,p}$:

$$J_w^s = \frac{\rho \varepsilon q_{sat}^w D_{wV}^s(0)}{\delta} (\theta_{w,f} - \theta_{w,p}) \quad (15)$$

Multiplying q_{sat}^w by the terms in the bracket, the final flux equation is:

$$J_w^s = \frac{\rho \varepsilon D_{wV}^s(0)}{\delta} (q_{w,f} - q_{w,p}) \quad (16)$$

Where $D_{w,f}^w$ and $D_{w,p}^w$ are the sorbet quantities of water into the zeolite at the feed and the permeate interfaces.

The above equation is based on the premise that transport of various species through a dense zeolite membrane follows the solution-diffusion mechanism. It should be mentioned that zeolite membranes obey a sorption-diffusion model like polymeric membranes. However, the ionic interactions are stronger in the case of zeolite membranes. The ionic interactions affect both the sorption and the diffusion of water into the membrane. For the zeolite membranes, a solution-diffusion mechanism can be envisioned wherein the water molecules first adsorb preferentially at the cage mouth and then diffuse across the active layer. For solvent molecules, however, the partial molecular sieving effects and permeation through non-zeolitic pores may also need to be considered. Therefore, a permeability parameter K_w can also be defined for water permeation through zeolite membranes in a similar manner as for polymeric membranes. The parameter is a lumped parameter comprising of the water diffusivity through the membrane, its sorption onto the membrane material and the membrane thickness.

The above equation also assumes that the permeability parameter remains constant under various feed concentrations and temperatures. However, this is not always true, especially in the case of polymeric membranes. For example, hydrophilic polymeric membranes tend to swell substantially in the presence of high water concentrations causing substantial changes in the permeability parameter of the polymer. The above model is a comprehensive modeling approach and gives helpful insights into the actual transport process within Nanopores of the zeolite (Hogendoom et al., 2001; Krishna and Paschek, 2002; Pera-Titus et al., 2006).

2. Materials and Methods

2.1. Support preparation

In this research, mullite supports were prepared from kaolin clay. Kaolin is thermally converted to mullite via high

temperature calcinations. The reaction takes place when kaolin is utilized as the sole source of silica and alumina. Free silica ($4SiO_2$) is generated as a result of this conversion. The free silica was leached out and then porous mullite bodies were prepared. Kaolin (SL-KAD grade) was supplied by WBB cooperation, England. The reaction can be represented by the following equation:



Analysis of the kaolin is listed in Table 2. Cylindrical shaped (tubular) bodies have been conveniently made by extruding a mixture of about 75-67% kaolin and 25-33% distilled water. Suitable calcinations temperatures and periods are those at which kaolin converts to mullite and free silica. Good results were achieved by calcinations for about 3 h at temperatures of about 1250 °C (Kazemimoghadam et al., 2006; Speronello, 1986a and 1986b).

Table 2. Analysis of kaolin clay

Component	Percent (%)	Phases	Percent (%)
SiO ₂	51.9	Kaolinite	79
TiO ₂	0.1	Illite	8
Al ₂ O ₃	34.1	Quartz	10
Fe ₂ O ₃	1.4	Feldspar	3
K ₂ O	0.8		
Na ₂ O	0.1	Total	100
L.O.I	11.6		
Total	100		

Free silica was removed from the calcined bodies after leaching by strong alkali solutions. Removal of the silica caused meso-porous tubular supports with very high porosity. Free silica removal was carried out using aqueous solutions containing 20% by weight NaOH at a temperature of 80 °C for 5 h. In order to remove all the remaining NaOH, supports were rinsed using huge amount of hot distilled water for a long time. Porosity of the supports before leaching was 24.3% while after treatment it increased to 49%. Flux of the supports before and after free silica removal at 1 bar and 20 °C was 6 kg/m²h and 10 kg/m²h, respectively. Porosity of the supports was measured by water absorption method. Phase identification was performed by X-ray diffraction with CuK_α radiation.

2.2. Zeolite membrane synthesis

2.2.1. Coating of the support with seeds

Adding seed crystals to this crystallization system resulted in increased crystallization rate. The enhanced rate might be due to simply increasing the rate at which solute is integrated into the solid phase from solution due to the increased available surface area, but also might be the result of enhanced nucleation of the new crystals. The secondary nucleation mechanism referred to as initial breeding results from microcrystalline dust being washed off seed crystal surfaces in a new synthesis batch. These microcrystalline fragments grew to observable sizes, and resulted in greatly enhanced crystallization rates due to remarkably increased crystal surface area compared to the unseeded system. Consequently, it is expected that addition of seed crystals to a synthesis system will introduce sub-micron sized crystallites into the system that will serve as nuclei.

As described above, porous mullite tubes (homemade) were used as the support. The external surface of the supports was polished with 600-grit sandpapers, and then the support was washed and cleaned with distilled water in a microwave heater for 5 min to remove loose particles created during polishing. Then, supports were dried at 100 °C for 3h. In order to form a thin and uniform zeolite membrane on the mullite support, the nucleation seeds should be small and uniform in size. In order to inhibit the formation of the zeolites into the support pores, the seeds should not penetrate into the pores. The high purity nucleation seeds were synthesized by hydrothermal method. Size of the seeds was about 2 μm . The seeds must be dispersed homogeneously on the support surface and the amount of seeds on the support surface must not be too much. Otherwise, the synthesized zeolite membrane is heterogeneous or too thick. The seeded supports were prepared by dipping the mullite supports in an 8% NaA zeolite suspension in a single step. The 8% NaA zeolite suspension was prepared by mixing 8 g NaA zeolite in 92 ml distilled water. After dipping procedure, the supports were dried at 100 °C for 3 h.

2.2.2. Nanopore NaA zeolite synthesis

Thin zeolite NaA membrane layers were grown hydrothermally over the external surface of the porous supports. Synthesis solution was prepared by mixing aluminates and silicate solutions. NaOH (4.87 g) was dissolved in 76 ml of distilled water. The solution was divided into two equal volumes and kept in polypropylene bottles. Aluminates solution was prepared by adding 6.23 g sodium aluminates (Aldrich, 50-56% Al_2O_3) to one part of the NaOH solution. It was mixed until cleared. Silicate solution was prepared by adding 16.57 g sodium silicate (Merck, 25-28% SiO_2) to another part of the NaOH solution. Silicate solution was then poured into aluminates solution and well mixed until a thick homogenized gel was formed. Composition of the homogeneous solution of zeolite NaA is represented by the following molar ratio: 1.926 SiO_2 : Al_2O_3 : 3.165 Na_2O : 128 H_2O (Malekpour et al., 2008; Aguado et al., 2009).

Two ends of the supports were closed with rubber caps to avoid any precipitation of the zeolite crystals on internal surface of the supports during membrane synthesis. The seeded supports were placed vertically in a Teflon autoclave. The solution was carefully poured in the autoclave and then the autoclave was sealed. Crystallization was carried out in an oven at temperatures of 70, 90, 100, 110 and 140 °C for 1, 2.5, 3, 4 and 5.5 h. Then, the samples were taken and the synthesized membranes were washed several times with distilled water. The samples were then dried at room temperature for 12 h in air. Some samples were coated two and three times to study effect of number of coating.

2.3. Pervaporation experiments

A pervaporation experimental set up was used to evaluate successful fabrication of NaA zeolite membranes.

Pervaporation experiments were carried out using a standard pervaporation apparatus. Feed solution, preheated to a constant temperature, was introduced to the outer side of the zeolite membrane in the pervaporation cell. The down-stream pressure was maintained at 133 Pa throughout the operation. The zeolite membranes were used for dehydration of aqueous ethanol mixtures. The ethanol mixtures (1,5,10,15 and 20 wt. %) were used and experiments were carried out at room temperature (25 °C) within a period of 30-60 min. Permeate concentrations were measured using GC (TCD detector, Varian 3400, carrier gas: hydrogen, column: polyethylene glycol, sample size: 5 micron, column and detector temperatures: 120-150 °C, detector flow rate: 15 ml/min, carrier flow: 5 ml/min, column pressure: 1.6 kPa, GC input pressure: 20 kPa).

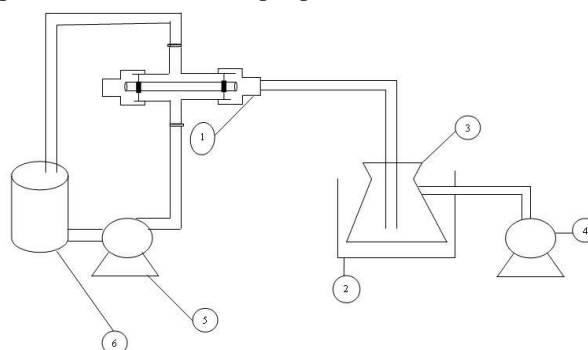


Fig. 2. Pervaporation setup; 1- Feed container and pervaporation cell, 2- Liquid nitrogen trap, 3- Permeate container, 4- Three stage vacuum pump, 5- Centrifuge pump, 6- Feed tank

Performance of pervaporation was evaluated using values of total flux ($\text{kg/m}^2\cdot\text{h}$) and separation factor (dimensionless). Typical experimental setup was employed as presented in Fig. 2. While pervaporation system was steady state (after 20 min), we measured weight of permeate after 30 min operation then flux was calculated (area of zeolite membrane is 44 cm^2). The change in feed concentration due to permeation was negligible because the amount of permeate was small compared to total liquid volume in the system (Bird et al., 1960; Malekpour et al., 2008; Aguado et al., 2009; Sorenson et al., 2011).

The phases Mullite, Cristobalite and SiO_2 identification was performed by XRD (Philips PW1710, Philips Co., Netherlands) with $\text{CuK}\alpha$ radiation. Morphology of the support and the membrane was examined by SEM (JEM-1200 or JEM-5600LV equipped with an Oxford ISIS-300 X-ray disperse spectroscopy (EDS)).

2.4. Water sorption experiments

The sorption experiments were performed using zeolite powder (200-mesh size). The zeolite powder in the presence of pure water forms a paste and it is very difficult to distinguish between the 'sorbet water' and the 'inter-particle water'. Thus, any sorption data based on gravimetric studies is not expected to be accurate. An indirect and more accurate method was employed to determine the pure water sorption of the zeolite powder. The zeolite powder was weighted and the powder was well mixed with a measured volume of the dilute ethanol

mixture (1, 5, 10, 15 and 20 wt. %). Equilibrium was established after 18–24 h. After the equilibrium, the mixtures were pressure filtered using a syringe. The water content was accurately measured. It was assumed that at such low ethanol concentrations, sorption of ethanol into the zeolite powder is negligible.

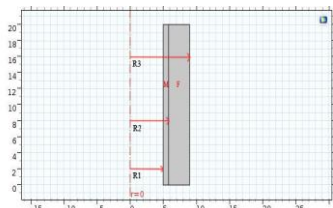


Fig. 3. Geometry of pervaporation system used in the simulation

2.4. FEM simulation

Fig. 3 represents the schematic diagram of the model domain used in the simulation. Feed solution containing a mixture of 1–20 wt. % ethanol flows tangentially through the upper side of the membrane system ($z = 0$). The feed exits at $z = L$ (membrane length) and recirculates inside the system.

The main assumptions to develop the numerical simulation are as follows: (1) Steady state and isothermal conditions, (2) No chemical reaction occurs in feed stream, (3) Feed solution flows only in the z direction, (4) Laminar feed flow in the membrane system, (5) Thermodynamic equilibrium considered at the interface of feed and membrane, (6) Small amount of ethanol permeates through the membrane, (7) Mass transfer resistance of the support layer was assumed to be negligible, (8) Fouling and concentration polarization effects on the pervaporation of ethanol-water solution are negligible, (9) The fluid is incompressible, and (10) Feed viscosity is constant.

Although the diffusive mass transfer in the direction of flow (z direction) is small due to the convective flux in this direction, it is not neglected compared to diffusive mass transfer in the r direction. Therefore, axial and radial diffusions inside the membrane and feed phase are considered in the continuity equations. Moreover, the small permeation of ethanol through the membrane is considered in the simulation by applying selectivity equation (Eq. (18)). The penetration of ethanol through the selective membrane is described by the following equation:

$$S = \frac{x_{\text{Ethanol}}}{x_{\text{water}}} \times \frac{y_{\text{water}}}{y_{\text{Ethanol}}} \quad (18)$$

The concentration of ethanol in the permeate side (y_{Ethanol}) must be determined by trial and error method. In this method, an initial value for y_{Ethanol} is guessed. Then the water concentration in the permeate side will be calculated using model equations. This calculated value then must be compared with the guessed value. If the difference between the old and new values is less than a determined error, the guessed ethanol concentration is considered as the correct concentration. Otherwise, another guess must be made for y_{Ethanol} . Mass transport in the membrane system is described using continuity equation. The following equation presents the differential form of this equation (Bird, 1960):

$$\frac{\partial C_w}{\partial t} + \nabla \cdot (-D_w \nabla C_w + U \cdot C_w) = R \quad (19)$$

where C_w denotes water concentration (mol/m^3), D_w denotes water diffusion coefficient (m^2/s), U denotes the velocity vector (m/s) and R denotes the reaction term ($\text{mol/m}^3 \cdot \text{s}$). Since no chemical reactions takes place in the ethanol/water pervaporation, the reaction term is zero. Continuity equation was defined and solved in COMSOL Multiphysics 5.2 by adding a “transport of diluted species” physic to the model domain. Velocity distribution was obtained by solving Navier-Stokes equations for momentum balance simultaneously with continuity equation in the feed side. This was done by adding a “laminar flow” physic to the whole model in COMSOL Multiphysics 5.2. The following equation describes the momentum conservation equation (Bird, 1960):

$$\rho \frac{\partial u}{\partial t} + \rho(u \cdot \nabla)u = \nabla \cdot [-P + \mu(\nabla u + (\nabla u)^T)] + F_b \quad (20)$$

$$\nabla \cdot (u) = 0 \quad (21)$$

where $u = z$ -component of the velocity vector (m/s), $\rho =$ feed density (kg/m^3), $P =$ pressure (Pa), $\mu =$ feed viscosity (Pa.s) and $F_b =$ a body force (N).

2.4.1. Feed phase simulation

By applying mentioned assumptions to the Eq. (19), steady state form of the continuity equation for water mass transport in the feed side is obtained:

$$-\frac{1}{r} \frac{\partial}{\partial r} \left(D_w r \frac{\partial C_{w-f}}{\partial r} \right) - \frac{\partial}{\partial z} \left(D_w \frac{\partial C_{w-f}}{\partial z} \right) + u \frac{\partial C_{w-f}}{\partial z} = 0 \quad (22)$$

The simplified form of the momentum transport equations considering above assumptions will be as follows:

$$\rho \left(u \frac{\partial u}{\partial z} \right) - \frac{1}{r} \frac{\partial}{\partial r} \left(r \mu \frac{\partial u}{\partial r} \right) - \frac{\partial}{\partial z} \left(\mu \frac{\partial u}{\partial z} \right) = -\frac{\partial P}{\partial z} \quad (23)$$

$$\frac{\partial u}{\partial z} = 0 \quad (24)$$

r and z denote radial and axial coordinates, respectively. The initial conditions for mass and momentum conservation equations are as below:

$$\text{at } t = 0, C_{w-f} = C_{0,w} \text{ and } u = u_0 \quad (25)$$

where C_{w-f} is water concentration in feed phase, $C_{0,w}$ is its initial value and u_0 is the initial velocity of the feed flow.

The boundary conditions for mass conservation equations in the feed phase are as follows:

$$\text{at } z = L, \text{ outflow condition} \quad (26)$$

$$\text{at } z = 0, C_{w-f} = C_{0,w} \text{ (Inlet boundary)} \quad (27)$$

$$\text{at } r = R_3, \frac{\partial C_{w-f}}{\partial r} = 0 \text{ (No flux condition)} \quad (28)$$

At the interface of the membrane-feed, the equilibrium condition is assumed:

$$\text{at } r = R_2, C_{w-f} = \frac{C_{w-m}}{n} \quad (29)$$

In which C_{w-m} is water concentration in membrane section and n is partition coefficient obtained from selectivity equation as follows:

$$n = \frac{y_{\text{Ethanol}}}{x_{\text{Ethanol}}} \times S = \frac{C_{w-m}}{C_{w-f}} \quad (30)$$

As mentioned earlier, permeate concentration of ethanol must be obtained using trial and error method and then

is placed in the above equation. The boundary conditions for momentum transfer equations are as follows:

$$\text{at } z = 0, u = u_0, \text{ (Inlet boundary)} \quad (31)$$

At the outlet, the pressure is atmospheric pressure:

$$\text{at } z = L, P = P_{\text{atm}}, \text{ (Atmospheric pressure)} \quad (32)$$

$$\text{At } r = R_2 \text{ and } R_3, u = 0 \text{ (No slip condition)} \quad (33)$$

2.4.2. Membrane phase simulation

Mass transport of water in the membrane is controlled only by diffusion mechanism. Therefore, the steady state continuity equation for water can be written as:

$$-\frac{1}{r} \frac{\partial}{\partial r} \left(D_m r \frac{\partial C_{w-m}}{\partial r} \right) - \frac{\partial}{\partial z} \left(D_m \frac{\partial C_{w-m}}{\partial z} \right) = 0 \quad (34)$$

where D_m is water diffusion coefficient in membrane (m^2/s).

Membrane phase boundary conditions are given as:

$$\text{at } r = R_2, C_{w-m} = n \times C_{w-f} \text{ (Equilibrium condition)} \quad (35)$$

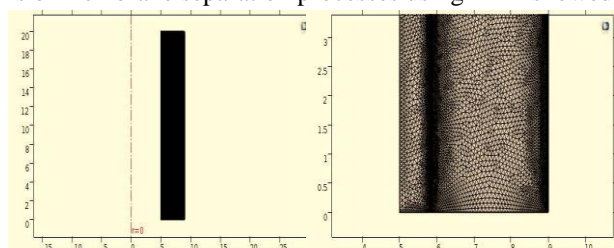
$$\text{at } r = R_1, C_{w-m} = 0 \text{ (Dry membrane condition)} \quad (36)$$

$$\text{at } z = 0 \text{ and } z = L, \frac{\partial C_{w-m}}{\partial z} = 0 \text{ (No flux condition)} \quad (37)$$

At the permeate-membrane interface, water concentration assumed to be zero due to the vacuum applied on this boundary.

2.4.3. Numerical solution of the conservation equations

Set of model equations, including mass and momentum transfer equations in the membrane module along with suitable boundary conditions was solved using COMSOL Multiphysics software version 5.2. The FEM is applied by this software to solve conservation equations numerically. Previous simulations of membrane separation processes using FEM showed



(a) Complete mesh (b) Magnification of a segment of the complete mesh

Fig. 4 Mesh used in the simulation; (a) Complete mesh and (b) Magnification of a segment of the complete mesh (Complete mesh consisted of 66007 domain elements and 1940 boundary elements)

that this method was an accurate, valid and powerful technique for solving mass and momentum equations (Rezazazemi et al., 2011; Moulik et al., 2015; Moulik et al., 2016). The computational time for solving the equations was about 2 minutes. "Extra fine" mesh was used in the simulation, which consisted of 66007 domain elements and 1940 boundary elements. Fig. 4 represents the meshes created by COMSOL Multiphysics 5.2 software. Due to the considerable difference between z and r dimensions, a scaling factor equal to 6 was

used in the z direction. Therefore, the results were reported in dimensionless length.

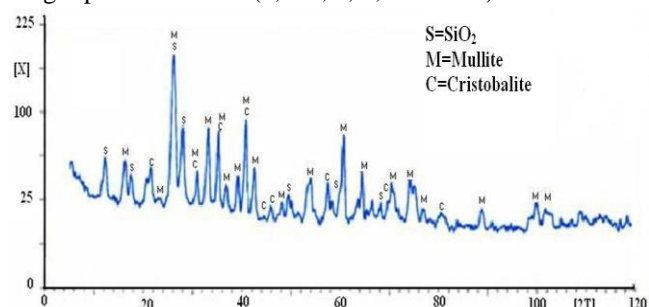
3. Results and Discussion

3.1. Effect of hydrothermal conditions on membrane formation and performance

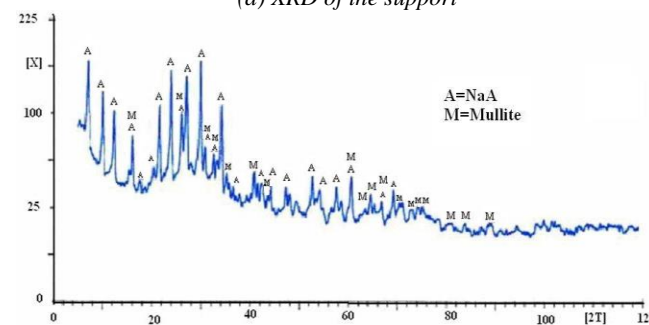
Temperature and time have a positive influence on the zeolite formation process, which occurs over a considerable range of temperatures. A rise in temperature will increase both the nucleation rate and the linear growth rate. Hence, the crystallinity of the samples normally increases in time. As far as time is concerned, zeolite synthesis is governed by the occurrence of successive phase transformations. The thermodynamically least favorable phase will crystallize first and will be successively replaced in time by more stable phases. The best example is the crystallization sequence of amorphous \rightarrow NaA \rightarrow HS.

The temperature, however, can also influence the type of product that has to be crystallized. A rise in temperature leads to the crystallization of more dense products as the fraction of water in the liquid phase, which has to stabilize the porous products by filling the pores, will drop. Therefore, the existence of an upper limit for the formation of zeolites is to be expected. The use of nonvolatile pore space occupying (filling) species would, in principle, allow a high-temperature synthesis of open, porous structures. Temperature can obviously affect the rate of nucleation and crystal growth.

The linear rates of crystal growth and rates of nucleation both increase with rising temperatures. To study effect of crystallization time and temperature on NaA zeolite membrane performance, the membranes were synthesized at different temperatures (70, 90, 100, 110, and 140 °C) over longer periods of time (1, 2.5, 3, 4, and 5.5 h).



(a) XRD of the support



(b) XRD of the NaA zeolite membrane

Fig. 5. XRD of the (a) Support and (b) NaA zeolite membrane

The kaolin after calcinations at 1250 °C for 3 h is converted into mullite and free silica. This shows that silica has been removed from the support. Removal of this free silica causes the support porosity to increase from 24.3% to 49%. Fig. 5 shows XRD patterns of the mullite support (Fig. 5(a)) and the zeolite NaA membrane (Fig. 5(b)). The XRD pattern of NaA zeolite membrane confirms that zeolite NaA crystals were formed. In these two figures, the only phases, which can be observed, are zeolite NaA and mullite. Fig. 6 shows SEM photographs of the mullite support (Fig. 6(a)) and the zeolite NaA membrane (Fig. 6(b) and (c)). Porous structure of the support and thin layer of the membrane can be easily observed.

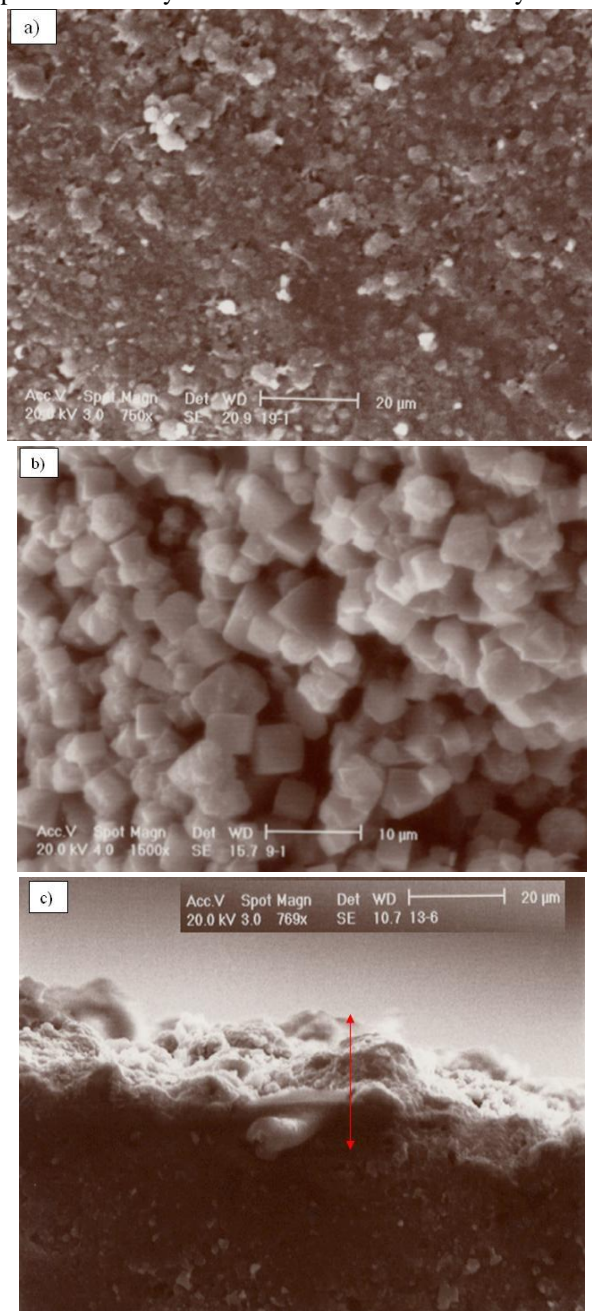


Fig. 6. SEM micrograph of the (a) Support, (b) Membrane (surface) and (c) Membrane (cross section)

The membranes were evaluated in a pervaporation setup as shown in Fig. 2. The synthesis procedure was also performed using different temperatures. As seen in Table 3, increasing crystallization temperature increases flux (samples

1, 2 and 3). In addition, it can be observed that there is no change in separation factor. This may be because at higher crystallization temperature, a thinner layer is formed. This is due to the fact that at higher temperatures, NaA zeolite crystals are smaller. This shows that these membranes have very high selectivity. The results show that a high temperature of 140 °C also results in zeolite NaA to be formed (sample 4). The crystallization temperature in a range of 70-140 °C was found to be very effective for making the NaA zeolite layer.

Table 3 Flux and separation factor of NaA zeolite membranes (dead

No.	Ethanol Con. (%)	$q_{w,f}$ kg/kg zeolite	J(Cal.) (kg/m ² .h)	J(Exp.) (kg/m ² .h)
1	1	0.594	0.337	0.331
2	5	0.567	0.321	0.311
3	10	0.521	0.295	0.279
4	15	0.493	0.279	0.258
5	20	0.452	0.256	0.229

end)*

A	B	C	D	E	F	G
1	1	3	70	90	0.0556	>10000
2	1	3	90	90	0.0602	>10000
3	1	3	110	90	0.0741	>10000
4	1	3	140	90	0.398	>10000
5	1	1	100	90	0.970	41
6	1	2.5	100	90	0.527	>10000
7	1	4	100	90	0.247	>10000
8	1	5.5	100	90	0.306	2

*A = Sample, B = Number of coating, C = Crystallization time (h), D = Crystallization temperature (°C), E = Concentration of ethanol in feed (wt %), F = Flux kg/m².h, G = Separation factor

As mentioned, the synthesis procedure was performed using different times. As seen in Table 3, over a longer period of crystallization time flux decreased (samples 6 and 7). However, there is no change in separation factor. This behavior may be attributed to the fact that at over an extended period of crystallization time, a thicker membrane layer is formed, which causes flux to reduce. This shows that these membranes behave very high selective. It must be mentioned that 20400 is the highest measurable value using the GC at 90 wt. % ethanol concentration. In this work, any test (preparation membrane and pervaporation test) carried out three times. The results show that short crystallization time (1 h) is not enough to make an effective zeolite layer on the support (sample 5). In addition, long crystallization time (5.5 h) causes NaA zeolite to transform to other zeolites such as NaX. As a result, this sample (8) shows poor selectivity. The crystallization time in a range of 2.5-4 h was found to be very effective for making the NaA zeolite layer. The results confirm that zeolite membranes synthesized at 110 °C for 3 h via a single stage process can be recommended for dehydration of ethanol-water mixtures.

3.2. Water flux calculation using S.M. Correlation

After water sorption experiments, Eq. (16) was employed to calculate diffusivity values of water through the zeolite matrix at 25 °C using water flux and sorption values at the same temperature. The diffusivity of pure water through the zeolite at 25 °C was computed (assuming $q_{w,p}=0$, $\rho_s=1990$ kg/m³, $\epsilon=0.49$ and $\delta=30$ μ m) to be 3.11×10^{-8} cm²/s (using experimental value of $J_w=0.22$ kg/m².h and $q_{w,f}=0.6$ kg/kg

zeolite at 25 °C). Sorption studies were also carried out using the zeolite NaA membrane. The zeolite membrane was crushed into fine pieces and the sorption experiments were performed in a similar manner as the powder. The sorption of the zeolite membrane was measured to be 0.29 kg/kg zeolite again indicating that the membrane is highly hydrophilic. This value is lower than the values of water sorption for the zeolite powder because of the backing material. The results of water flux calculations are also presented in Table 4.

Table 4. Experimental and calculated data from S.M. equation

Comparison of experimental water fluxes and calculated water fluxes by S.M. correlation are demonstrated in Table 4 and Fig. 7. Variation of the experimental flux through the zeolite membranes and the calculated flux with water concentration in the feed mixtures was shown. As seen in Table 4 and Fig. 7, reduction of water content in the mixture causes the water flux to decrease. As seen, the experimental and calculated data are consistent.

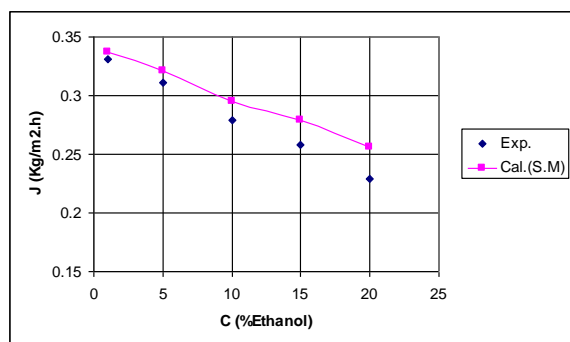


Fig. 7. Water flux as a function of ethanol concentration

3.3. FEM simulation results

3.3.1. Water concentration distribution

Fig. 8 (a) and (b) illustrates surface water concentration distribution within two sub-domains of the membrane and feed, respectively. Ethanol-water solution containing 20 wt. % ethanol flows over the outer surface of the membrane module ($z = 0$). Concentration profile within the feed side was measured by simultaneous solution of the continuity equations of mass and momentum using COMSOL Multiphysics software version 5.2. FEM was applied by this software for numerical solution of the conservation equations. As observed, a concentration boundary layer is formed on the membrane-feed interface in feed compartment (Fig. 8 (b)). At

$z = 0$, the water concentration is maximum (80 wt. %). As the feed solution flows in the feed compartment, water moves towards the membrane surface due to the concentration and pressure differences (driving forces). Water concentration on the membrane surface is less than its value at the feed inlet (where water concentration is equal to its initial value, $C_{0,w}$).

In fact, the water concentration on the membrane surface was calculated from the membrane selectivity (Eq. 29) and its value in the membrane side. Since water concentration in membrane is always less than its value in the feed section, the water concentration on the membrane-feed boundary ($r = R_2$) is always less than its value in the feed bulk.

Water transfer mechanism through the membrane was described only by diffusion. Since at the membrane-permeate interface the vacuum condition was imposed, the water concentration on this boundary was measured to be zero (Fig. 8 (a)). Water distribution is highest on the membrane-feed interface, because it is obtained from its value in the feed part, which is always highest (Eq. (35)).

Fig. 9 represents the effect of various membrane lengths on the water concentration versus r -coordinate at constant temperature, flow rate and ethanol initial concentration of 25 °C, 3 liter/min and 20 wt. %, respectively. Water concentration increases along r direction, as expected. The concentration gradient in feed compartment (Fig. 9 (b)) is great at regions near the membrane-feed interface ($r = R_2$) due to the mass transfer towards the membrane at this region (greater driving force). Concentration reaches a constant value ($C_{0,w} = 80$ wt. %) at radii more than 6.5 mm. At regions near the feed entrance ($z = 30$ mm) total concentration is higher. This is because that this region is near the feed flow inlet with maximum concentration value ($C_{0,w} = 80$ wt. %). Water distribution within the membrane (Fig. 9 (a)) is linear. Its concentration is zero on the membrane-permeate boundary because of the dry membrane assumption applied on this boundary. This is due to the fact that the water is vaporized on this region and its concentration reaches zero. Water concentration is highest on feed-membrane interface, as mentioned above.

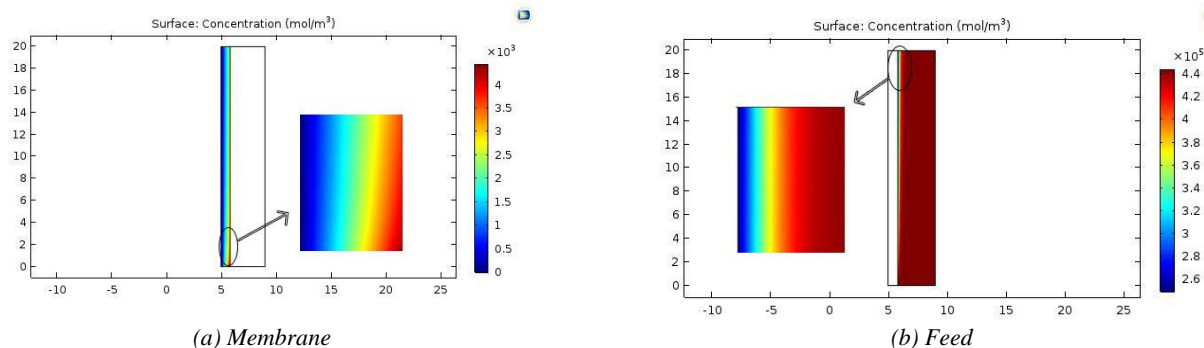


Fig. 8. Concentration distribution of water at 25 °C temperature and 3 liter/min feed flow rate (20 wt. % initial concentration of ethanol); (a) Membrane section and (b) Feed section

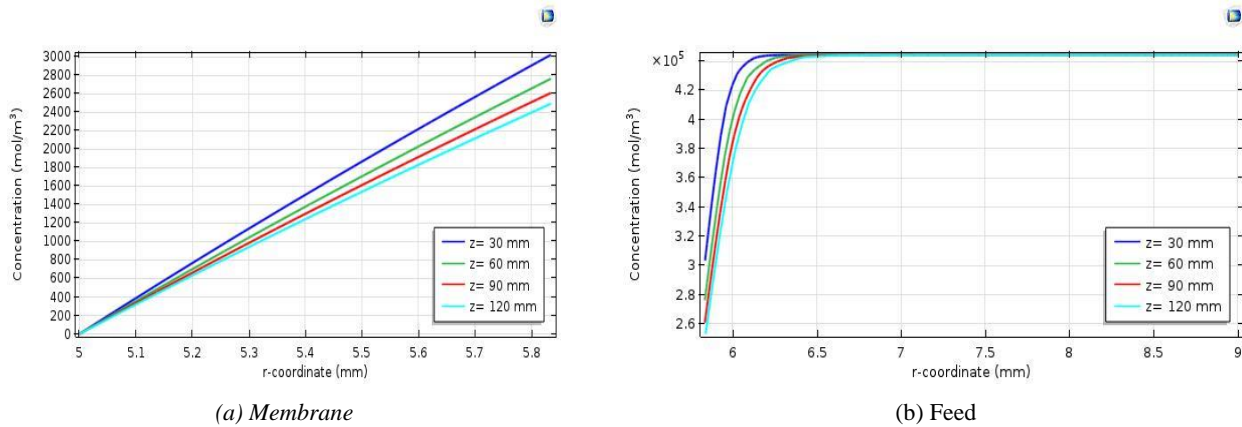


Fig. 9. Water concentration profile vs. r -coordinate at different membrane lengths (25 °C temperature, 20 wt. % initial concentration of ethanol and 3 liter/min feed flow rate); (a) Membrane section and (b) Feed section

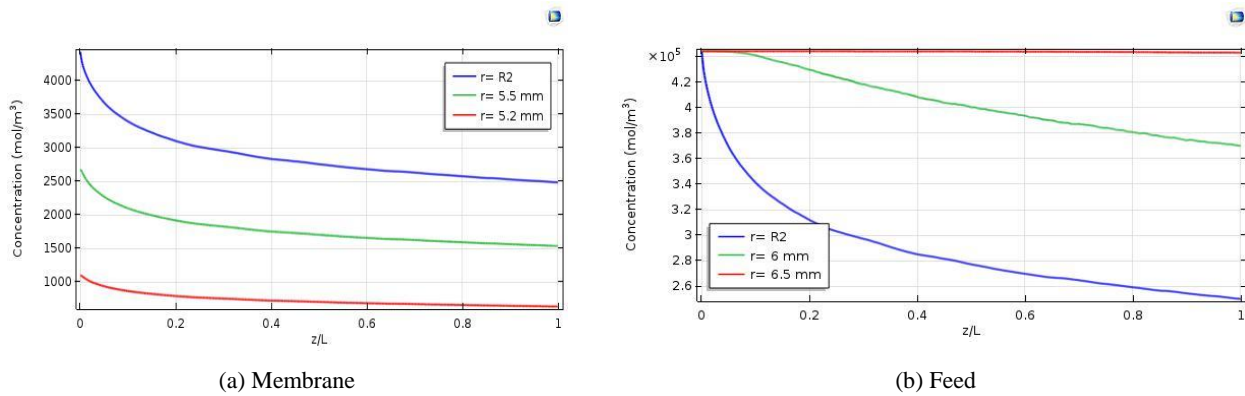


Fig. 10. Water concentration distribution vs. dimensionless length at different radii (25 °C temperature, 20 wt. % initial concentration of ethanol and 3 liter/min feed flow rate); (a) Membrane section and (b) Feed section

Fig. 10 demonstrates the concentration profile along z coordinate at constant flow rate (3 liter/min) and different radii. Results indicate that the variation of water concentration along the z coordinate is considerable and that cannot be neglected compared to its variation along r coordinate. The figure also illustrates that the concentration value is greater at membrane module entrance, which is due to the higher water concentrations at feed inlet. By moving away from the membrane-feed interface within feed section ($r > R_2$ in Fig. 10 (b)), the concentration increases. This behavior can be attributed to less water transfer towards the membrane at regions far from membrane-feed boundary, which will consequently result in much higher concentration values. Similarly, water distribution within the membrane (Fig. 10

(a)) is higher at areas near the feed-membrane interface ($R = R_2$).

Figs. 11 and 12 show the effect of various feed flow rates on water concentration distribution within the feed and the membrane section. As can be seen, water concentration increases with growing feed flow rate. This behavior can be attributed to the fact that higher velocities (or flow rates) would decrease the contact time of the feed stream with membrane and consequently less water has enough time to pass through the membrane. Therefore, much higher concentrations will be obtained at feed compartment and at larger feed flow rates. Similarly, concentration profile grows in membrane segment (according to Eq. (35)). Hence, it can be concluded that the effective flow rate is 3 liter/min.

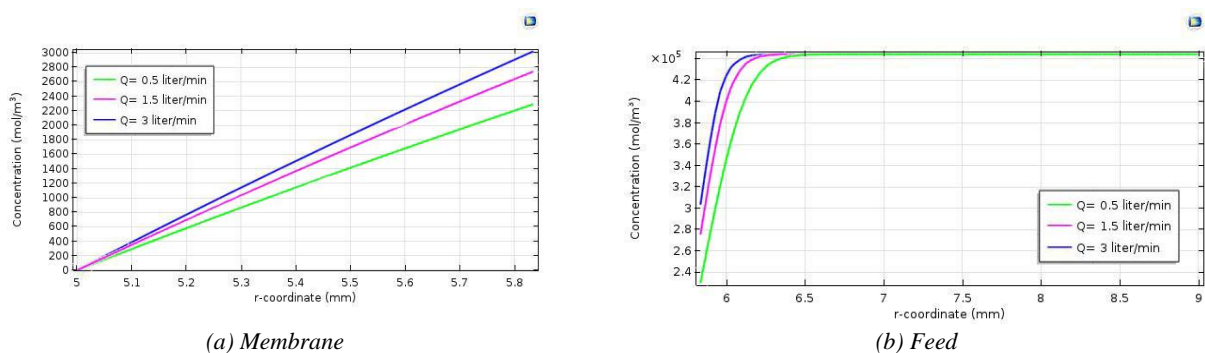


Fig. 11. Water concentration profile vs. r -coordinate at different feed flow rates (25 °C temperature and 20 wt. % initial concentration of ethanol); (a) Membrane section and (b) Feed section

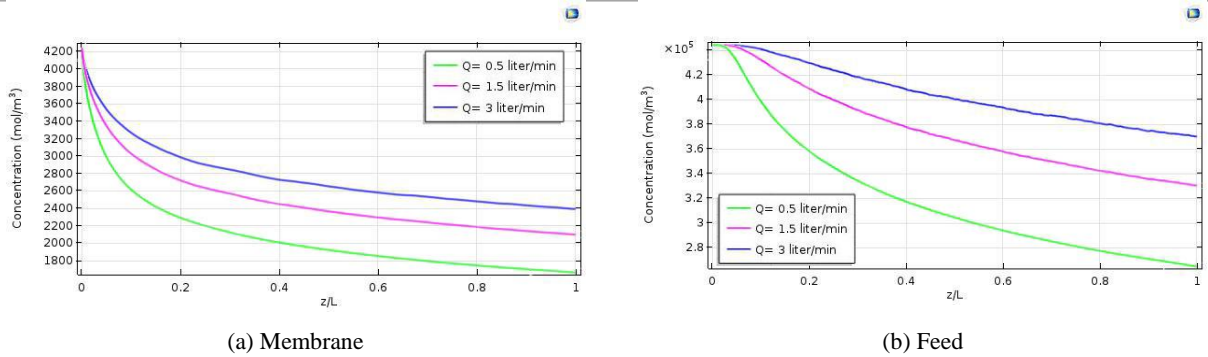


Fig. 12. Water concentration profile vs. membrane dimensionless length at different feed flow rates (25 °C temperature and 20 wt. % initial concentration of ethanol); (a) Membrane section and (b) Feed section

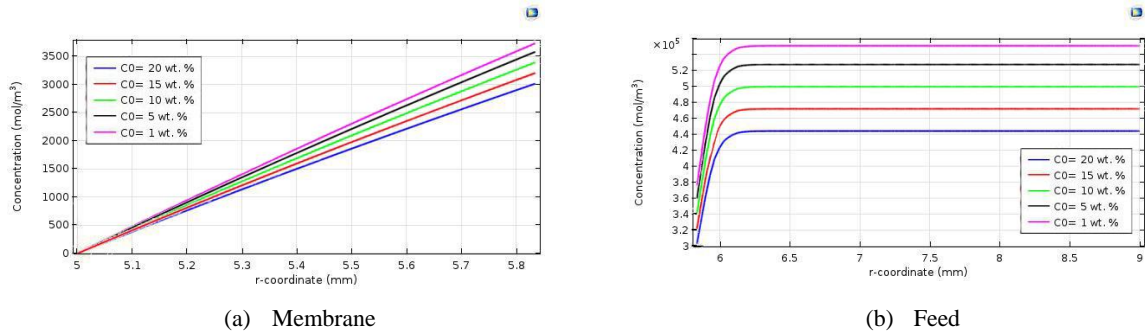


Fig. 13. Water concentration profile within the membrane vs. r-coordinate at different ethanol concentrations (3 l/min feed flow rate and 25 °C temperature); (a) Membrane section and (b) Feed section

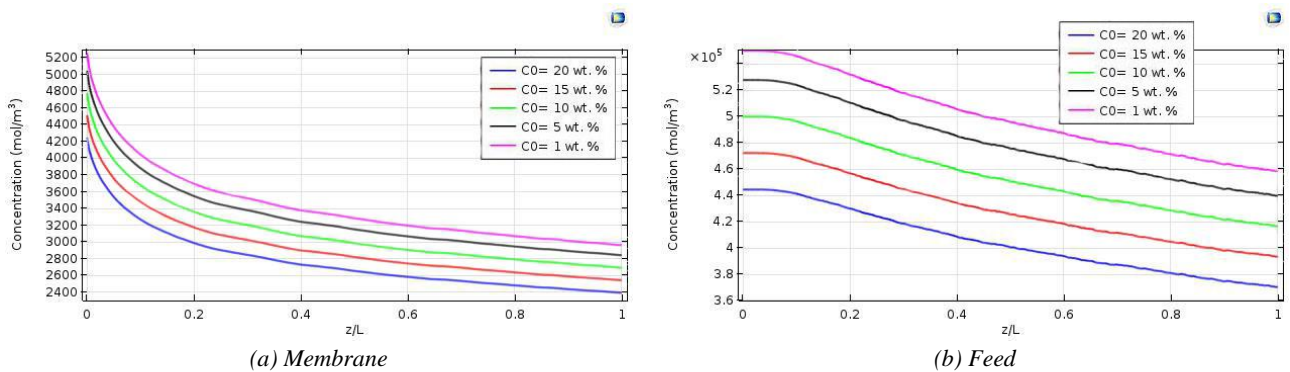


Fig. 14. Water concentration profile vs. membrane dimensionless length at different ethanol concentrations (3 liter/min feed flow rate and 25 °C temperature); (a) Membrane section and (b) Feed section

Figs. 13 and 14 show the effect of ethanol initial concentration in feed stream on water concentration. With increasing the initial ethanol concentration, water concentration decreases, as expected. It can be concluded that the optimum ethanol concentration is 1 wt. % at 25 °C.

3.3.2. Velocity distribution

Fig. 15 shows the velocity field in the feed phase of the pervaporation membrane system. The velocity distribution was obtained using numerical solution of momentum balance. This was done by adding a “laminar flow” physic to the whole model in COMSOL. As can be seen from the Fig. 15, the velocity profile is fully developed after a short distance. Velocity is zero on the membrane-feed interface and the outer radius of feed section (due to no slip condition on these boundaries) and is highest on the half of the feed section (symmetry condition).

Fig. 16 shows the effect of various membrane lengths on the velocity profile vs. radius in the feed subdomain.

According to the Fig. 16, the velocity profile is parabolic and becomes fully developed after a short distance (lengths approximately more than 18 mm). As observed, entrance effects are considered in this simulation, which is one of the advantages of FEM simulation.

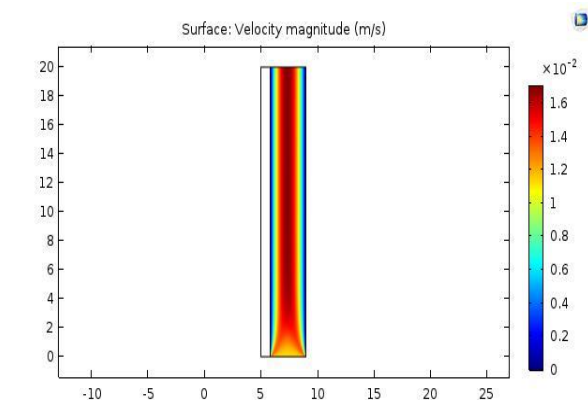


Fig. 15 Velocity profile (25 °C temperature, 3 liter/min feed flow rate and 20 wt. % initial concentration of ethanol)

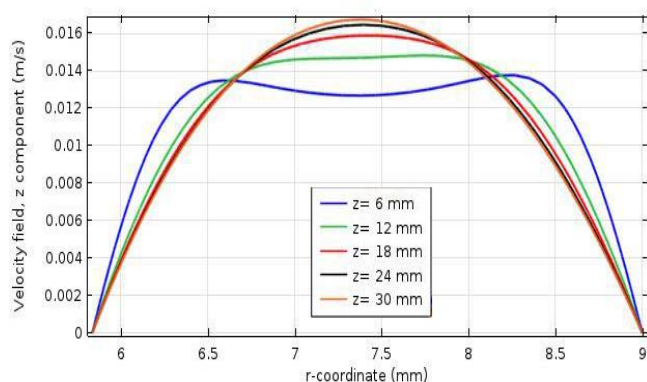


Fig. 16. Velocity profile vs. *r*-coordinate at different membrane lengths (25 °C temperature, 3 liter/min feed flow rate and 20 wt. % initial concentration of ethanol)

Fig. 17 represents the effect of varying feed flow rates on the velocity distribution vs. dimensionless length. Velocity profile is almost parabolic and reaches its maximum value at the regions close to the feed entrance. Maximum velocity magnitude increases with increasing feed flow rate, as expected.

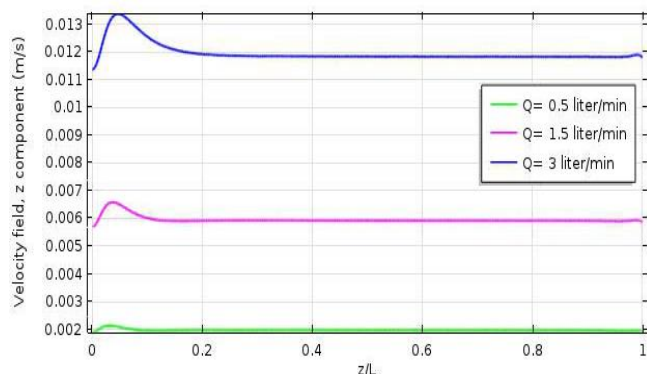


Fig. 17. Velocity profile vs. dimensionless membrane length at different feed flow rates (25 °C temperature and 20 wt. % initial concentration of ethanol)

4. Conclusion

Zeolite membranes have great potential for applications in ethanol dehydration. Zeolite NaA membranes were synthesized on the porous mullite tubes by hydro-thermal method. The best range operating condition (time and temperature) for hydrothermal synthesis of nanopore NaA zeolite membrane were 2.5-4 h and 70-140 °C, respectively. The presented two models are comprehensive modeling approaches and give helpful insights into the actual transport process within nanoporous NaA membranes. Pervaporation separation of the zeolite NaA membranes was studied over a broad range of concentrations and temperatures for binary solvent–water systems. Very high water–solvent separation factors were obtained over the entire range of concentration for all ethanol–water mixtures. High separation factors can be explained in terms of the strong interaction between the water molecules and the ionic sites in the zeolite crystal lattice and the partial sieving achieved by the zeolite channels. In addition, the water flux through the membrane was found to be almost independent on the ethanol concentration (at high water concentrations 80–100 wt. %), implying that the water transport through the membrane is uncoupled. The distinct

advantages offered by inorganic zeolite membranes, are their high solvent resistance and no swelling tendency. Due to these properties, it is possible to use these membranes with a variety of solvents and over a broad spectrum of process conditions and temperatures. Thus, it is possible to use these membranes under conditions where the polymeric membranes cannot be used due to high swelling, membrane instability or low selectivity. By making zeolites with different cage sizes or different cationic species, it may be possible to tailor these membranes for specific purposes such as organic–organic separations and membrane reactor applications.

References

- Aguado S, Gascón J, Jansen JC, and Kapteijn F. 2009. Continuous synthesis of NaA zeolite membranes. *Microporous and Mesoporous Materials* 120(1-2): 170–176. DOI: <https://doi.org/10.1016/j.micromeso.2008.08.062>
- Amnuaypanich S, J. Patthana J, and Phinyocheep P. 2009. Mixed matrix membranes prepared from natural rubber/poly(vinyl alcohol) semi-interpenetrating polymer network (NR/pervaporation. A semi-IPN) incorporating with zeolite 4A for the pervaporation dehydration of water–ethanol mixtures. *Chemical Engineering Science* 64(23): 4908 – 4918. DOI: <https://doi.org/10.1016/j.ces.2009.07.028>
- Bird RB, Stewart WE, and Lightfoot EN. *Transport phenomena*, John Wiley & Sons, New York, 1960, 2nd edition.
- Das P and Ray SK. 2013. Analysis of sorption and permeation of acetic acid–water mixtures through unfilled and filled blend membranes. *Separation and Purification Technology* 116: 433-447. DOI: <https://doi.org/10.1016/j.seppur.2013.06.003>
- Das P and Ray SK. 2016. Pervaporation recovery of tetrahydrofuran from water with plasticized and filled polyvinylchloride membranes. *Journal of Industrial and Engineering Chemistry* 34: 321-336. DOI: <https://doi.org/10.1016/j.jiec.2015.12.007>
- Díaz VH and Tost GO. 2016. Butanol production from lignocellulose by simultaneous fermentation, saccharification, and pervaporation or vacuum evaporation. *Bioresource Technology* 218: 174-182. DOI: <https://doi.org/10.1016/j.biortech.2016.06.091>
- Hogendoorn JA, van der Veen AJ, van der Stegen JHG, Kuipers JAM, and Versteeg GF. 2001. Application of the Maxwell–Stefan theory to the membrane electrolysis process Model development and simulations. *Computers and Chemical Engineering* 25(9-10): 1251–1265. DOI: [https://doi.org/10.1016/S0098-1354\(01\)00697-4](https://doi.org/10.1016/S0098-1354(01)00697-4)
- Hoof VV, Dotremont C, and Buekenhoudt A. 2006. Performance of Mitsui NaA type zeolite membranes for the dehydration of organic solvents in comparison with commercial Polymeric pervaporation membranes. *Separation and Purification Technology* 48(3): 304–309. DOI: <https://doi.org/10.1016/j.seppur.2005.06.019>
- Jain M, Attarde D, and Gupta SK. 2017. Removal of thiophenes from FCC gasoline by using a hollow fiber pervaporation module: Modeling, validation and influence of module dimensions and flow directions. *Chemical Engineering Journal* 308: 632-648. DOI: <https://doi.org/10.1016/j.cej.2016.09.043>
- Jiang J, Wang L, Peng L, Cai C, Zhang C, Wang X, and Gu X. 2017. Preparation and characterization of high performance CHA zeolite membranes from clear solution. *Journal of Membrane*

- Science 527: 51-59. DOI: <https://doi.org/10.1016/j.memsci.2017.01.005>
- Kazemimoghadam M, Pak A, and Mohammadi T. 2004. Dehydration of water/1-1-dimethylhydrazine mixtures by zeolite membranes. *Microporous and Mesoporous Materials* 70(1-3): 127-134. DOI: <https://doi.org/10.1016/j.micromeso.2004.02.015>
- Krishna R and Paschek D. 2002. Verification of the Maxwell–Stefan theory for diffusion of three-component mixtures in zeolites. *Chemical Engineering Journal* 87(1): 1–9. DOI: [https://doi.org/10.1016/S1385-8947\(01\)00187-5](https://doi.org/10.1016/S1385-8947(01)00187-5)
- Klinov AV, Akberov RR, Fazlyev AR, and Farakhov MI. 2017. Experimental investigation and modeling through using the solution-diffusion concept of pervaporation dehydration of ethanol and isopropanol by ceramic membranes HybSi. *Journal of Membrane Science* 524: 321-333. DOI: <https://doi.org/10.1016/j.memsci.2016.11.057>
- Kondo M and Kita H. 2010. Permeation mechanism through zeolite NaA and T-type membranes for practical dehydration of organic solvents. *Journal of Membrane Science* 361(1-2): 223–231. DOI: <https://doi.org/10.1016/j.memsci.2010.05.048>
- Lin L, Zhang Y, and Kong Y. 2009. Pervaporation separation of n-heptane-thiophene mixtures by polyethylene glycol membranes: Modeling and experimental. *Journal of Colloid and Interface Science* 339 (1): 152-159. DOI: <https://doi.org/10.1016/j.jcis.2009.07.015>
- Liu D, Liu G, Meng L, Dong Z, Huang K, and Jin W. 2015. Hollow fiber modules with ceramic-supported PDMS composite membranes for pervaporation recovery of bio-butanol. *Separation and Purification Technology* 146: 24-32. DOI: <https://doi.org/10.1016/j.seppur.2015.03.029>
- Liu G, Jiang Z, Cao K, Nair S, Cheng X, Zhao J, Goma H, Wu H, and Pan F. 2017. Pervaporation performance comparison of hybrid membranes filled with two-dimensional ZIF-L nanosheets and zero-dimensional ZIF-8 nanoparticles. *Journal of Membrane Science* 523: 185-196. DOI: <https://doi.org/10.1016/j.memsci.2016.09.064>
- Li Q, Cheng L, Shen J, Shi J, Chen G, Zhao J, Duan J, Liu G, and Jin W. 2017. Improved ethanol recovery through mixed-matrix membrane with hydrophobic MAF-6 as filler. *Separation and Purification Technology* 178: 105-112. DOI: <https://doi.org/10.1016/j.seppur.2017.01.024>
- Li Y, Chen H, Liu J, Li H, and Yang W. 2007. Pervaporation and vapor permeation dehydration of Fischer–Tropsch mixed-alcohols by LTA zeolite membranes. *Separation and Purification Technology* 57(1): 140–146. DOI: <https://doi.org/10.1016/j.seppur.2007.03.027>
- Malekpour A, Millani MR, and Kheirkhah M. 2008. Synthesis and characterization of a NaA zeolite membrane and its applications for desalination of radioactive solutions. *Desalination* 225(1-3): 199–208. DOI: <https://doi.org/10.1016/j.desal.2007.02.096>
- Moulik S, Kumar KP, Bohra S, and Sridhar S. 2015. Pervaporation performance of PPO membranes in dehydration of highly hazardous MMH and UDMH liquid propellants. *Journal of Hazardous Materials* 288: 69-79. DOI: <https://doi.org/10.1016/j.jhazmat.2015.02.020>
- Moulik S, Nazia S, Vani B, and Sridhar S. 2016. Pervaporation separation of acetic acid/water mixtures through sodium alginate/polyaniline poly ion complex membrane. *Separation and Purification Technology* 170: 30-39. DOI: <https://doi.org/10.1016/j.seppur.2016.06.027>
- Narkkun T, Jenwiriyakul W, Amnuaypanich S. 2017. Dehydration performance of double-network poly(vinyl alcohol) nanocomposite membranes (PVAs-DN). *Journal of Membrane Science* 528: 284-295. DOI: <https://doi.org/10.1016/j.memsci.2016.12.069>
- Nour M, Kosaka H, Bady M, Sato S, and Abdel-Rahman AK. 2017. Combustion and emission characteristics of DI diesel engine fueled by ethanol injected into the exhaust manifold. *Fuel Processing Technology* 164: 33-50. DOI: <https://doi.org/10.1016/j.fuproc.2017.04.018>
- Pera-Titus M, Llorens J, Tejero J, and Cunill F. 2006. Description of the pervaporation dehydration performance Of A-type zeolite membranes: A modeling approach based on the Maxwell–Stefan theory. *Catalysis Today* 118(1-2): 73–84. DOI: <https://doi.org/10.1016/j.cattod.2005.12.006>
- Pera-Titus M, Llorens J, Tejero J, Cunill F. 2006. Description of the pervaporation dehydration performance Of A-type zeolite membranes: A modeling approach based on the Maxwell–Stefan theory. *Catalysis Today* 118(1-2): 73–84. DOI: <https://doi.org/10.1016/j.cattod.2005.12.006>
- Qiao Z, Wu Y, Li X, and Zhou J. 2011. Molecular simulation on the separation of water-ethanol azeotropic mixture by poly(vinyl alcohol) membrane. *Fluid Phase Equilibria* 302(1-2): 14-20. DOI: <https://doi.org/10.1016/j.fluid.2010.09.045>
- Qu H, Kong Y, Lv H, Zhang Y, Yang J, D. Shi D. 2010. Effect of crosslinking on sorption, diffusion and pervaporation of gasoline components in hydroxyethyl cellulose membranes. *Chemical Engineering Journal* 157(1): 60-66. DOI: <https://doi.org/10.1016/j.cej.2009.09.044>
- Rezakazemi M, Shahverdi M, Shirazian S, Mohammadi T, and Pak A. 2011. CFD simulation of water removal from water/ethylene glycol mixtures by pervaporation. *Chemical Engineering Journal* 168(1): 60-67. DOI: <https://doi.org/10.1016/j.cej.2010.12.034>
- Rom A, Miltner A, Wukovits W, and Friedl A. 2016. Energy saving potential of hybrid membrane and distillation process in butanol purification: Experiments, modeling and simulation. *Chemical Engineering and Processing* 104: 201-211. DOI: <https://doi.org/10.1016/j.cep.2016.03.012>
- Samei M, Iravaninia M, Mohammadi T, and Asadi AA. 2016. Solution diffusion modeling of a composite pervaporation/fumed silica ceramic supported membrane. *Chemical Engineering and Processing: Process Intensification* 109: 11-19. DOI: <https://doi.org/10.1016/j.cep.2016.06.002>
- Santoro S, Galiano F, Jansen JC, and Figoli A. 2017. Strategy for scale-up of SBS pervaporation membranes for ethanol recovery from diluted aqueous solutions. *Separation and Purification Technology* 176: 252-261. DOI: <https://doi.org/10.1016/j.seppur.2016.12.018>
- Sato K, Sugimoto K, and Nakane T. 2008. Preparation of higher flux NaA zeolite membrane on asymmetric porous support and permeation behavior at higher temperatures up to 145°C in vapor permeation. *Journal of Membrane Science* 307(1): 181–195. DOI: <https://doi.org/10.1016/j.memsci.2007.09.017>
- Sorenson SG, Payzant EA, Gibbons WT, Soydas B, Kita H, Noble RD, and Falconer LL. 2011. Influence of zeolite crystal expansion/contraction on NaA zeolite membrane separations.

- Journal of Membrane Science 366(1-2): 413–420. DOI: <https://doi.org/10.1016/j.memsci.2010.10.043>
- Sorenson SG, Payzant EA, Gibbons WT, Soydas B, Kita H, Noble RD, and Falconer JL. 2011. Influence of zeolite crystal expansion/contraction on NaA zeolite membrane separations. *Journal of Membrane Science* 366(1-2): 413–420. DOI: <https://doi.org/10.1016/j.memsci.2010.10.043>
- Speronello K. 1986a- Porous mullite, U.S. Patent NO 4628042.
- Speronello K. 1986b- Porous mullite, U.S. Patent No. 4601997.
- Xia LL, Li CL, Wang Y. 2016. In-situ crosslinked PVA/organosilica hybrid membranes for pervaporation separations. *Journal of Membrane Science* 498: 263-275. DOI: <https://doi.org/10.1016/j.memsci.2015.10.025>
- Yin H, Lau CY, Rozowski M, Howard C, Xu Y, Lai T, Dose ME, Lively RP, Lind ML. 2017. Free-standing ZIF-71/PDMS nanocomposite membranes for the recovery of ethanol and 1-butanol from water through pervaporation. *Journal of Membrane Science* 529: 286-292. DOI: <https://doi.org/10.1016/j.memsci.2017.02.006>
- Yu L, Zeng C, Wang C, and Zhang L. 2017. In situ impregnation–gelation–hydrothermal crystallization synthesis of hollow fiber zeolite NaA membrane. *Microporous and Mesoporous Materials* 244: 278-283. DOI: <https://doi.org/10.1016/j.micromeso.2016.10.047>

Conflict of interest: Non declare